Atomic Structure of Ultrathin Gold Nanowires

Yi Yu,[1,2] Fan Cui,[1,2] Jianwei Sun,[1,2] and Peidong Yang [1,2,3,4]*

[1]Department of Chemistry, University of California, Berkeley, California 94720, United States

[2]Materials Science Division, Lawrence Berkeley National Laboratory, Berkeley, California 94720, United States

[3]Kavli Energy NanoScience Institute, Berkeley, California 94720, United States

[4]Department of Materials Science and Engineering, University of California, Berkeley, California 94720, United States

ABSTRACT:

Understanding of the atomic structure and stability of nanowires (NWs) is critical for their applications in nanotechnology, especially when the diameter of NWs reduces to ultrathin scale (1~2 nm). Here, using aberration-corrected high-resolution transmission electron microscopy (AC-HRTEM), we report a detailed atomic structure study of the ultrathin Au NWs, which are synthesized using a silane-mediated approach. The NWs contain large amounts of generalized stacking fault defects. These defects evolve upon sustained electron exposure and simultaneously the NWs undergo necking and breaking. Quantitative strain analysis reveals the key role of strain in the breakdown process. Besides, ligand-like morphology is observed at the surface of the NWs, indicating the possibility of using AC-HRTEM for surface ligand imaging. Moreover, the coalescence dynamic of ultrathin Au NWs is demonstrated by in-situ observations. This work provides a comprehensive understanding of the structure of ultrathin metal NWs at atomic-scale and could have important implications for their applications.

KEYWORDS: Ultrathin Au nanowires, aberration-corrected high-resolution transmission electron microscopy, defect, strain, surface ligand, coalescence

Ultrathin Au nanowires (NWs) (~ 2 nm) are of great interests for nanoscience researches as well as for nanotechnology applications[1-4]. Owing to the high surface area and quantum-confined diameter, they have been demonstrated to present intriguing properties, such as quantum conductance and ballistic conduction[5, 6]. Synthesis of high quality single crystalline ultrathin Au NWs is critical to the physical property measurements and other application studies. A flurry of reports has come out recently, regarding the successful synthesis of ultrathin Au NWs[1-4, 7]. However, the challenge in yield and quality control still exists, and the growth mechanisms are not always clear[1]. There is still plenty of room for the improvement and pursuing of optimal growth conditions. On the other hand, the challenge facing the structure characterization is significant. Imaging of the ultrathin NWs by high-resolution transmission electron microscopy (HRTEM) is difficult, as they tend to break under the electron beam[6, 8, 9], which sometimes has rendered the high quality atomic-scale imaging almost impossible[1]. The breakdown of ultrathin Au NWs has attracted both experimental and theoretical research interests[6, 9-13]. In many of the previous experimental studies, the Au NW was introduced by focusing the electron beam near the holes of self-supported Au film and nanometric constrictions (i.e. bridges) could be formed between the holes[6, 10, 11]. Strictly speaking, these so-called NWs were not actual NWs. Instead, they were short nanobridges. The experimental setup is good for electrical measurements of quantum properties of the ultrathin chains but may not fully represent the structural behavior of true NWs[5, 6]. Meanwhile, the theoretical simulations only considered the situation of perfect single crystalline NW[12, 13], which may not always be correct for the actual solution-synthesized products. Structural defects as well as surface ligands should exist in most real systems. Therefore, a direct structural study of the as-synthesized ultrathin Au NWs is needed. Sparse reports[9, 14, 15] were demonstrated very recently, revealing the structural features of the as-synthesized ultrathin Au NWs, including the transient state of NW breakdown with single-atom chain[9], the local lattice strain[14], and the wrinkling of atomic planes[15]. However, detailed static structure (defects, surface ligands) and the dynamic behavior (breakdown, atomic diffusion), as well as the correlation of defects, strain, and the NW breakdown remain to be understood.

Here, we report a detailed atomic structure analysis of the ultrathin Au NWs, which are synthesized using a silane-mediated approach, with oleylamine as shaping surfactants. Atomic character of the NW can be clearly resolved by taking advantage of the aberration-corrected HRTEM (AC-HRTEM)[16]. Analysis of the stacking sequence of atomic planes indicates the NWs are highly defective. Interestingly, the defects evolve upon sustained electron exposure. Simultaneously, the NWs undergo necking and breaking process. A quantitative two-dimensional atomic-scale strain mapping can help understand these structure evolutions. Besides, ligand-like long-chain morphology is observed at the surface of the NWs and the possibility of surface ligand imaging is discussed. Finally, the coalescence dynamic of ultrathin Au NWs is demonstrated via in-situ atomic-scale observation.

Sub-two nanometer ultrathin Au NWs were successfully synthesized in our early report[4]. Herein, we have further developed the synthetic procedure, and large yield, high quality ultrathin Au NWs can be grown more efficiently through the current silane-mediated recipe (See supporting information for details. The silane-mediated recipe was also reported by another group[17]). The growth process and the possible mechanism are summarized in Figure 1a. When $HAuCl_4 \cdot 3H_2O$ is mixed with oleylamine, oleylamine can serve as a coordinating ligand and these two will form Au (III)-oleylamine complex. The solution has a clear orange color. After several tens of minutes, the Au (III) complex will be gradually reduced to a Au(I) form, which is indicated by an orange-to-light yellow color transition. Silane, which can be used as mild reducing agents for metal nanomaterial synthesis[18], is introduced to our system as an additional reducing agent besides oleylamine. Triisopropylsilane is selected for the purpose of gold reduction for its mild reducing power and non-air sensitive nature. Under the reaction condition, Au (I) complex are slowly reduced to Au metallic form. Due to the presence of oleylamine and its preferential attachment towards Au {100} facets, gold starts to grow into one-dimensional nanorods within the mixture. Since the Au {100} surfaces are heavily protected with oleylamine molecules, the incoming Au atoms will be forced to deposit at the end of the rods, promoting one-dimensional growth to later become long nanowires. In addition, we also believe that oriented attachment also happens in the nanowire growing process. Two ends of the nanorods or shorter nanowires could merge together

and form a long, single nanowire. This is evidenced by our TEM results, which will be discussed later. Figure 1b shows the low-magnification TEM image of the as-synthesized ultrathin Au NWs. Large yield ultrathin Au NWs with uniform diameter (~ 2 nm) and micrometer length were obtained. For even lower magnification TEM images, one may refer to Figure S1.

The atomic structure characterization was performed using AC-HRTEM (TEAM 0.5) at an accelerating voltage of 80 kV, which can reduce the knock-on damage of Au[9]. The structural evolution under the low voltage is affected by the radiolysis damage. The usage of monochromator together with an inserted slit narrows the energy spread, allows for variation of the electron dose rate as well as the control of beam-illuminating area[19, 20]. In this case, the structural evolution of ultrathin Au NWs can be controlled to the specific nano-region and at a moderate rate so that the camera can capture the process clearly in the time-scale of seconds. Figure 1c represents a typical AC-HRTEM image of one of the ultrathin Au NWs. Under the negative spherical-aberration imaging condition[16, 21, 22], the Au atom columns appear bright on a dark background. All of the Au atom columns are well resolved in the [110] projection. A section of the NW (in red box) is enlarged and shown in Figure 1d. In order to better understand the atomic feature, we have performed image simulation based on the structural model of a perfect face-centered-cubic (FCC) Au NW with similar diameter as the experimental one. The image was simulated under similar microscope operation conditions, using the multislice method[23] as implemented in the MacTempas software[24] (See supporting information for details). The corresponding simulated image and structural model are shown in Figure 1e and 1f, respectively. Excellent agreement is achieved between the experimental image and the simulation. As can be seen, the NW is grown along the <111> direction, and the FCC structure of the Au NW is represented by the stacking of {111} planes in the sequence of ABCABC along the axial direction. Looking into Figure 1d, one may notice that the atomic columns in individual {111} lattice planes do not stay in straight horizontal lines as in Figure 1e. Such deviations from their ideally equilibrium positions indicates the wrinkling feature of the {111} planes[15]. Looking back to a larger field of vision as in Figure 1c, an interesting feature is that the surface of the ultrathin Au NW is not smooth as it comes to the atomic level. Instead, atomic steps/kinks form the wavy surface.

To perform an in-depth structural study, we analyzed the stacking sequence of the {111} planes line by line through the whole NW in view in Figure 1c and the result is shown in Figure 2a. In the top region, the stacking sequence follows the perfect FCC stacking of ABCABC. However, in the rest part of the NW, lots of defects exist. In FCC metals, twin boundary (TB) and stacking fault (SF) are the commonly found defects. All these defects can be described as the so-called generalized stacking fault (GSF). TB is the boundary that above and below which the atomic configurations are related to each other via a mirror plane reflection, while SF can be further classified as intrinsic SF (ISF) and extrinsic SF (ESF). ISF has the stacking sequence of ABCABABC, with removal of one of the close-packed planes. In opposite, ESF represents the insertion of one extra plane, making the sequence as ABCBABC. For both ISF and ESF, there is a local hexagonal close-packed (HCP) environment around the faulted plane. Continuous packing of ISF or ESF will result in a hexagonal phase, in the sequence of ABAB or ABCBABCB, which is denoted as 2H or 4H structure[25, 26]. In our case, although there are AB and ABCB segments, they do not form continuous long-distance stacking so that we assign these defects as ISF and ESF (Figure 2a). Therefore, the ultrathin Au NW is still in FCC phase, however, contains large amount of GSF defects. The formation of densely faulted {111} planes is closely related to the growth process of the ultrathin Au NW, further supporting the previous proposed oriented attachment mechanism[7, 8].

Considering that the faulted planes will induce local distortions, strain distribution and relaxation becomes another point worthy of study. One may even imagine that the strain relaxation could relate to the structure instability and NW breakdown. To pinpoint the relationship between defect and strain, as well as their influence on the NW instability, we exposed the ultrathin Au NW under continuous electron beam illumination with moderate dose rate so that the structure evolution occurred slowly such that we were able to capture the process with sequential frames. Figure 2a is the first image we captured, serving as a starting point. During the electron beam illumination, shearing of {111} atomic planes occurred at different spots of the NW and gradually necking was formed, and then followed by sudden structural relaxations the NW broke at two necks, leaving three segments in the view of the imaging area as shown in Figure 2c. It is worth mentioning that the exact moment of breakdown was not easy to capture and different

NWs could have different breakdown configurations[9]. Furthermore, the sudden structural relaxations are always accompanied with local tilting of parts of the NW (one example with large tilting is shown in Figure S2) so that the images taken during the breaking can not represent all the atom positions accurately. Therefore, in order to quantify the atom positions accurately and make our defect/strain analysis universal, we only compared the images before (Figure 2a) and after breakdown (Figure 2c) and ignored the dynamic process in between. Moreover, to relax the structure more completely, the NW was deliberately exposed for a period of time after breakdown and the image is shown in Figure 2e. In the original status (Figure 2a), the NW contained perfect FCC stacking as well as all kinds of GSF (TB, ISF and ESF). After breakdown (Figure 2c), the top segment turned to perfect FCC stacking, while the rest two segments exhibited ISF and ESF. The quantity of ISF and ESF decreased and more TBs appeared after further relaxation (Figure 2e). Correspondingly, the strain evolution during the breakdown process was shown in Figure 2b, d, and f. To achieve quantitative strain analysis at the atomic-scale, first, the positions of the contrast maxima in the AC-HRTEM images, corresponding to the atomic positions, were determined by a least-squares fit of the intensity distribution using two-dimensional Gaussian profiles[22]. Then the area of each triangle unit bounded by three nearest Au atom columns was measured. Finally the area values were converted to strain values[27] with respect to the ideal bulk Au lattice parameters.

Combining with first-principle calculations based on the density-functional theory (DFT), the defect evolution can be understood from the energy point of view. The DFT calculation was performed using the ABINIT code[28] with the Troullier-Martins pseudopotential within the local density approximation (See supporting information for details). Table 1 shows the defect energies of ISF, ESF and TB, respectively. It is obvious that the TB energy is typically lower than the other two, in agreement with the empirical approximation relation of $E_{ISF} \approx E_{ESF} \approx 2E_{TB}$[29, 30]. The lower energy of TB indicates that it is more favorable than ISF and ESF, as can be seen from Figure 2a. Given enough period of time for the relaxation, the relatively unstable ISF and ESF tend to automatically convert to TB (Figure 2c, 2e) to further lower the system energy. According to the defect analysis of several NWs, it is found that the NW does not always break at certain type of GSF

defects. It seems that the type of defects (either unfavorable ISF, ESF or favorable TB) is not a direct factor causing the NW breakdown. We propose that the strain is likely to be a key factor. From the original strain mapping (Figure 2b), it is shown that there is no obvious strain inhomogeneity along the NW. Most of the random distributed local strain appears at the surface, which is attributed to the surface reconstruction[14]. Two areas with relative dense strain are indicated by circles, both of which suffer from ~10% tensile strain (blue color). These two areas are later shown to be the breakpoints of the NW. Meanwhile, the two areas are also the necks of the NW, with smaller local diameters (6~7 atom columns wide) than the other parts (8~9 atom columns wide). The strain became larger and inhomogeneous right after breakdown, accompanied by diameter expansion (Figure 2d). After further relaxation, the strain could be relaxed to some extent while certain local surface strain still existed (Figure 2f). Based on the above results, we discuss about the breakdown mechanism of ultrathin Au NWs. Macroscopically, the breakdown of Au NW can be described by the capillary effect or so-called Rayleigh instability[31, 32], as already been demonstrated in thick metal wires[32]. The Rayleigh instability is based on a simple geometric argument that the cylinder has a larger surface area than the row of spheres/droplets so that it will evolve to many small droplets to lower the free energy of the system. For ultrathin Au NW, it should still obey the universal rule of capillarity-induced shape change in liquid jets and cylindrical solids. However, the Rayleigh instability does not tell us how and where the local breaking occurs, whereas our atomic direct observations enable to answer the question. Atomically, the ultrathin Au NW breaks at the necks originally formed during the growth, where the local dense tensile strain exists. After breakdown, the NW tends to relax the strain by diameter expansion and shearing of atomic planes (this will cause defect evolution). It is worth mentioning that the status in Figure 2e and 2f should not be the final equilibrium state. By virtue of the surface tension, the Au segments tend to further minimize their surface area. Given enough long period of time, it is believed that the ultrathin Au NW may break into a chain of Au spheres (Figure S3).

Another interesting but less studied point in nanostructure characterization is the surface ligand. It is quite common that wet chemical synthesis use organic surfactants to protect, modulate, and stabilize nanocrystals. In the case of ultrathin metal NWs, the ligands play

a particularly important role in confining the growth direction and determining the final morphology[4, 18]. Consequently, observing the ligands is helpful for exploring the growth mechanism as well as understanding the electronic and optical properties of the whole nanosystem[33]. However, direct imaging of ligands is a very difficult task and has not been well solved yet, mainly because of the beam-sensitive nature of the organic surfactants. Moreover, the strong contrast coming from the nanocrystals makes it more difficult to see the weak-contrast surfactants as well as the soft-hard interfaces. To our best knowledge, graphene is one of the most suitable supporting membranes that may enable the ligand imaging as it provides the lowest background noise[34]. Taking advantage of the ultrathin graphene membrane and the minimization of delocalization effect in AC-HRTEM[16], we have attempted to image the oleylamine ligands on the ultrathin Au NW surface and the results are shown in Figure 3. To enhance the contrast of surface ligands, the images were processed using contrast equalization algorithm and then false-colored[33]. Three pieces of evidence suggest the existence of surface ligands. Firstly, as shown in Figure 3a, it is commonly observed that ultrathin Au NWs aligned in parallel. The distance between two neighboring NWs is about 2 nm. The existence of surface ligands in between can explain such NW separation. However, a single stretched oleylamine is about 2 nm in length, which indicates that most of the ligands are confined to a region less than 1 nm from the surface, warping around the surface of the NWs[33]. Secondly, looking into the structural detail on the NW surface, we observe some chain-like feature. One example is shown in Figure 3b, which is the enlarged view of the boxed region in Figure 3a. Chain-like features are indicated by the dot lines. For comparison, a simulated image of a single stretched oleylamine attached on ultrathin Au NW surface is shown in Figure 3c. Finally, the ligands can be evidenced by in-situ observation of the NW surface morphology evolution. Figure 3d and 3e are two images from an in-situ time series acquisition, showing the same area as in Figure 3a. Under the electron beam, two NWs in the middle of Figure 3a began to break and the moving directions of three fracture tips are indicated in Figure 3d and 3e, respectively. In early stage, three tips began to move towards the edge of the image, and a small area of single-layer graphene was exposed (Figure 3d). The area of the graphene extended as the tips kept moving. Assuming the surface ligands were closely attached the surface, they would also move following the tips, leaving the

underneath graphene exposed (Figure 3e). Another similar in-situ observation of chain-like feature evolution is shown in Figure S4. It is consistently observed that the contrast of the chain-like features becomes stronger under continuous electron beam illumination. It is probably because of continuous absorption of carbon contamination onto the ligands and the ligand intertwining.

Finally, the coalescence of ultrathin Au NWs is studied through in-situ AC-HRTEM observations. The results are shown in Figure 4. In the early stage (Figure 4a), two neighboring NWs broke into several segments, as we have discussed previously. After exposure to the electron beam for some time, it is possible that more and more surface ligands of the small segments were damaged and metal surface began to expose. Two segments shown in Figure 4b started to get closer to each other and surface diffusion occurred. Inset is the enlarged image of the boxed region, clearly showing the atomic channels of surface diffusion. This is the direct evidence that the coalescence is driven by the surface mass diffusion[35]. The right tips of the segments were then connected (Figure 4c) and gradually two segments were fully merged (Figure 4d). The atomic planes of the as-merged nanoparticle (NP) were not nicely matched and misfit dislocations existed (indicated by the red arrow). Then the NP could release the strain and misfit by self-adjustment and finally defect-free NP could be formed (Figure 4e). As higher resolution imaging is still lacking in the studies of metal NP coalescence phenomenon[35-37], our atomic-scale direct observations clearly reveal the process, further confirming the surface diffusion mechanism[35].

In summary, ultrathin Au NWs have been successfully and efficiently synthesized via a novel, silane-mediated approach. Detailed atomic structure study of ultrathin Au NWs has been carried out using AC-HRTEM combined with image simulations and first-principle calculations. The ultrathin Au NWs exhibit atomic wavy surface and contain large amounts of defects (ISF, ESF and TB). The defects evolve upon sustained electron exposure and simultaneously the NWs undergo necking and breaking process. The breakdown process and the final morphology are mainly governed by the strain effect. Besides, ligand-like long-chain morphology is observed at the surface of the NWs, indicating the possibility of using AC-HRTEM for surface ligand imaging. Moreover, the coalescence dynamic of ultrathin Au NWs is demonstrated by in-situ observation at

atomic-scale. The overall structural study of ultrathin Au NWs provides a structural framework for understanding of structure-property relationship at the atomic-scale, paving the way towards application of ultrathin Au NWs on nanotechnology.

ASSOCIATED CONTENT

Supporting Information

Supplementary data contain low magnification images of ultrathin Au NWs, breakdown of the NW with twist, NW morphology after breakdown, and in-situ observation of dynamic behavior of surface ligands. Ultrathin Au NW synthesis, AC-HRTEM image simulation and first-principle calculation details are also provided. This material is available free of charge via the Internet at http://pubs.acs.org.

AUTHOR INFORMATION

Corresponding Author

*E-mail: p_yang@berkeley.edu.

Author Contributions

Y.Y. carried out the AC-HRTEM experiments, image simulations, DFT calculations, and data analysis. F.C., and J.S. performed nanowires fabrication. P.Y. supervised the research work. Y.Y., F.C., and P.Y. wrote the paper. All the authors discussed the results and commented on the manuscript.

Notes

The authors declare no competing financial interest.

ACKNOWLEDGMENTS

This work was supported by the Office of Science, Office of Basic Energy Science, of the U.S. Department of Energy under Contract No. DE-AC02-05CH11231 (PChem). We thank Dr. Linhan Lin and Dr. Jie Ma for discussion on DFT calculations. Work at the NCEM, Molecular Foundry was supported by the Office of Science, Office of Basic

Energy Science, of the U.S. Department of Energy under Contract No. DE-AC02-05CH11231.

REFERENCES

1. Cademartiri, L.; Ozin, G. A. *Adv. Mater.* **2009,** 21, 1013-1020.
2. Lu, X.; Yavuz, M. S.; Tuan, H. -Y.; Korgel, B. A.; Xia, Y. *J. Am. Chem. Soc.* **2008,** 130, 8900-8901.
3. Wang, C.; Hu, Y.; Lieber, C. M.; Sun, S. *J. Am. Chem. Soc.* **2008,** 130, 8902-8903.
4. Huo, Z.; Tsung, C. K.; Huang, W.; Zhang, X.; Yang, P. *Nano Lett.* **2008,** 8, 2041-2044.
5. Ohnishi, H.; Kondo, Y.; Takayanagi, K. *Nature* **1998,** 395, 780-783.
6. Rodrigues, V.; Fuhrer, T.; Ugrate, D. *Phys. Rev. Lett.* **2000,** 85, 4124-4127.
7. Halder, A.; Ravishankar, N. *Adv. Mater.* **2007,** 19, 1854-1858.
8. Kura, H.; Ogawa, T. *J. Appl. Phys.* **2010,** 107, 074310.
9. Lacroix, L. M.; Arenal, R.; Viau, G. *J. Am. Chem. Soc.* **2014,** 136, 13075-13077.
10. Rodrigues, V.; Ugarte, D. *Phys. Rev. B* **2001,** 63, 073405.
11. Lagos, M. J.; Sato, F.; Galvao, D. S.; Ugarte, D. *Phys. Rev. Lett.* **2011,** 106, 055501.
12. da Silva, E. Z.; Novaes, F. D.; da Silva, A. J. R.; Fazzio, A. *Phys. Rev. B* **2004,** 69, 094116.
13. Park, H. S.; Zimmerman, J. A. *Phys. Rev. B* **2005,** 72, 054106.
14. Kundu, P.; Turner, S.; Van Aert, S.; Ravishankar, N.; Van Tendeloo, G. *ACS Nano* **2014,** 8, 599-606.
15. Roy, A.; Kundu, S.; Muller, K.; Rosenauer, A.; Singh, S.; Pant, P.; Gururajan, M. P.; Kumar, P.; Weissmuller, J.; Singh, A. K.; Ravishankar, N. *Nano Lett.* **2014,** 14, 4859-4866.
16. Urban, K. W. *Science* **2008,** 321, 506-510.
17. Feng, H.; Yang, Y.; You, Y.; Li, G.; Guo, J.; Yu, T.; Shen, Z.; Wu, T.; Xing, B. *Chem. Commun.* **2009**, 1984-1986.
18. Cui, F.; Yu, Y.; Dou, L.; Sun, J.; Yang, Q.; Schildknecht, C.; Schierle-Arndt, K.; Yang, P. *Nano Lett.* **2015,** 15, 7610-7615.
19. Barton, B.; Jiang, B.; Song, C.; Specht, P.; Calderon, H.; Kisielowski, C. *Microsc. Microanal.* **2012,** 18, 982-994.
20. Kisielowski, C.; Specht, P.; Gygax, S. M.; Barton, B.; Calderon, H. A.; Kang, J. H.; Cieslinski, R. *Micron* **2015,** 68, 186-193.
21. Jia, C. L.; Lentzen, M.; Urban, K. *Science* **2003,** 299, 870-873.
22. Yu, Y.; Zhang, X.; Zhao, Y. G.; Jiang, N.; Yu, R.; Wang, J. W.; Fan, C.; Sun, X. F.; Zhu, J. *Appl. Phys. Lett.* **2013,** 103, 032901.
23. Cowley, J. M., *Diffraction Physics*. Elsevier: Amsterdam, 1995.
24. O'Keefe, M. A.; Kilaas, R. *Scan. Microsc. Suppl.* **1988,** 2, 225-244.
25. Huang, X.; Li, S.; Huang, Y.; Wu, S.; Zhou, X.; Li, S.; Gan, C. L.; Boey, F.; Mirkin, C. A.; Zhang, H. *Nature commun.* **2011,** 2, 292.

26. Fan, Z.; Bosman, M.; Huang, X.; Huang, D.; Yu, Y.; Ong, K. P.; Akimov, Y. A.; Wu, L.; Li, B.; Wu, J.; Huang, Y.; Liu, Q.; Png, C. E.; Gan, C. L.; Yang, P.; Zhang, H. *Nature commun.* **2015,** 6, 7684.
27. Gan, L.; Yu, R.; Luo, J.; Cheng, Z.; Zhu, J. *J. Phys. Chem. Lett.* **2012,** 3, 934-938.
28. Gonze, X.; Amadon, B.; Anglade, P. M.; Beuken, J. M.; Bottin, F.; Boulanger, P.; Bruneval, F.; Caliste, D.; Caracas, R.; Côté, M.; Deutsch, T.; Genovese, L.; Ghosez, P.; Giantomassi, M.; Goedecker, S.; Hamann, D. R.; Hermet, P.; Jollet, F.; Jomard, G.; Leroux, S.; Mancini, M.; Mazevet, S.; Oliveira, M. J. T.; Onida, G.; Pouillon, Y.; Rangel, T.; Rignanese, G. M.; Sangalli, D.; Shaltaf, R.; Torrent, M.; Verstraete, M. J.; Zerah, G.; Zwanziger, J. W. *Comput. Phys. Commun.* **2009,** 180, 2582-2615.
29. Finkenstadt, D.; Johnson, D. D. *Phys. Rev. B* **2006,** 73, 024101.
30. Bernstein, N.; Tadmor, E. B. *Phys. Rev. B* **2004,** 69, 094116.
31. Rayleigh, L. *Proc. London Math. Soc.* **1878,** s1-10, 4-13.
32. Karim, S.; Toimil-Molares, M. E.; Balogh, A. G.; Ensinger, W.; Cornelius, T. W.; Khan, E. U.; Neumann, R. *Nanotechnology* **2006,** 17, 5954-5959.
33. Gunawan, A. A.; Chernomordik, B. D.; Plemmons, D. S.; Deng, D. D.; Aydil, E. S.; Mkhoyan, K. A. *Chem. Mater.* **2014,** 26, 3328-3333.
34. Lee, Z.; Jeon, K. J.; Dato, A.; Erni, R.; Richardson, T. J.; Frenklach, M.; Radmilovic, V. *Nano Lett.* **2009,** 9, 3365-3369.
35. Jose-Yacaman, M.; Gutierrez-Wing, C.; Miki, M.; Yang, D. -Q.; Piyakis, K. N.; Sacher, E. *J. Phys. Chem. B* **2005,** 109, 9703-9711.
36. Chen, Y.; Palmer, R. E.; Wilcoxon, J. P. *Langmuir* **2006,** 22, 2851-2855.
37. Lim, T. H.; McCarthy, D.; Hendy, S. C.; Stevens, K. J.; Brown, S. A.; Tilley, R. D. *ACS Nano* **2009,** 3, 3809-3813.

FIGURES & TABLES

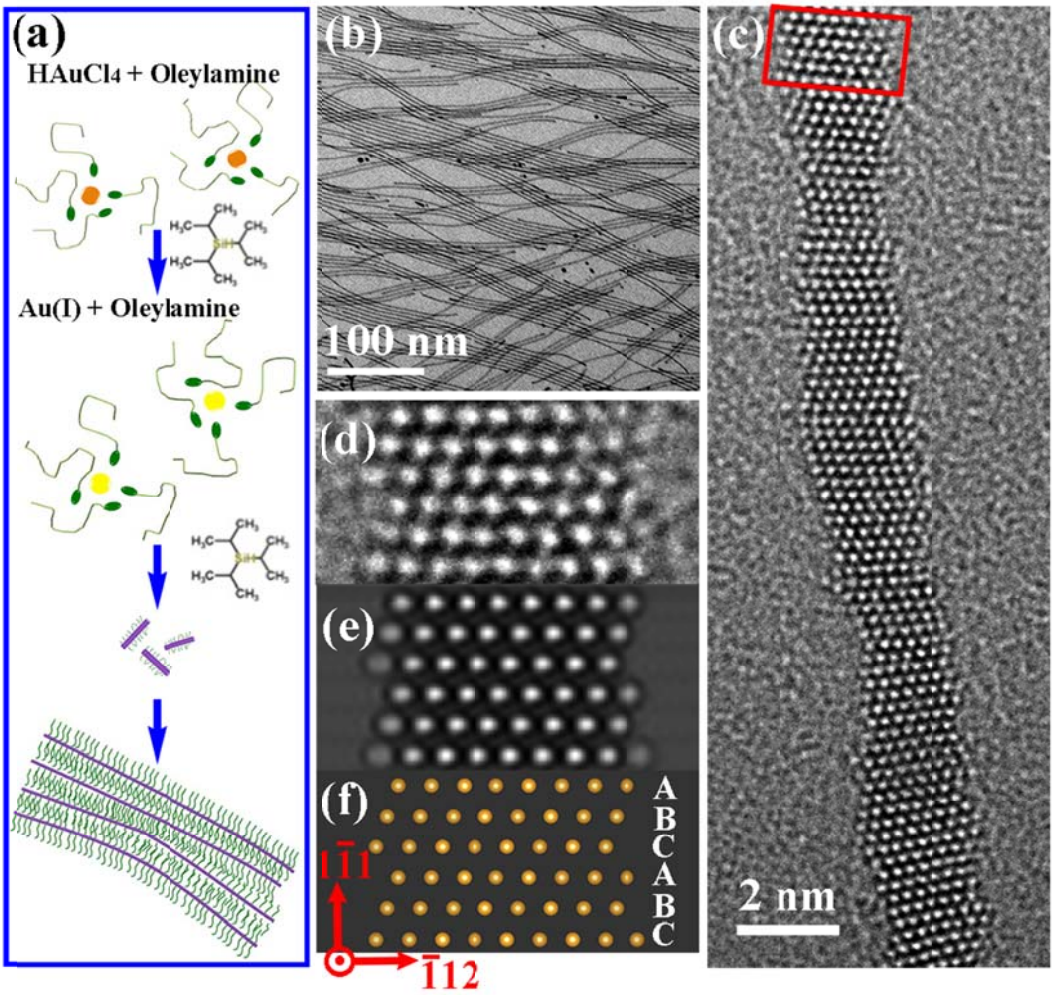

Figure 1. Synthesis and characterization of ultrathin Au NWs. (a) Schematic illustration for the synthesis of ultrathin Au NWs. (b) Low magnification TEM image and (c) AC-HRTEM image of ultrathin Au NWs. (d) Enlarged image of the boxed region in (c), with corresponding (e) simulated image and (f) structure model in the [110] zone axis.

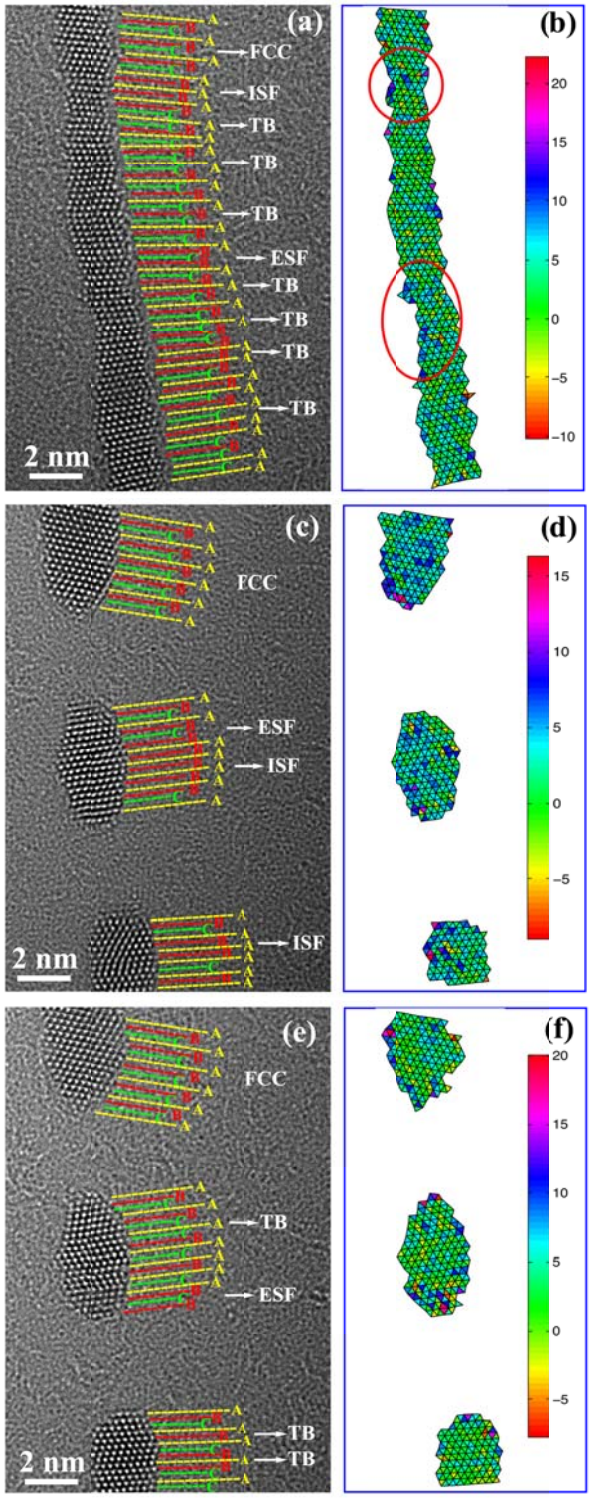

Figure 2. Defect and strain analysis of the ultrathin Au NW. AC-HRTEM images of the Au NW (a) before breakdown, (c) after breakdown, and (e) after further relaxation. The corresponding atomic-scale strain mappings are shown in (b), (d), and (f), respectively. The color scale bars indicate the stain in persentage (%). Stacking sequence of the {111} atomic planes and different types of GSF defects are labeled in AC-HRTEM images (a, c, e). The red circles in (b) indicate the necking positions with inhomogeneous strain.

Table 1. Comparison of defect energies of ISF, ESF, and TB in FCC Au given by first-principle calculations. Based on the interpolation method proposed in Ref. 29, supercells with 14, 13, and 18 layers are used for calculating the energies of ISF, ESF, and TB, respectively.

Defect Type	**ISF**	**ESF**	**TB**
Energy (mJ/m^2)	**41**	**49**	**19**

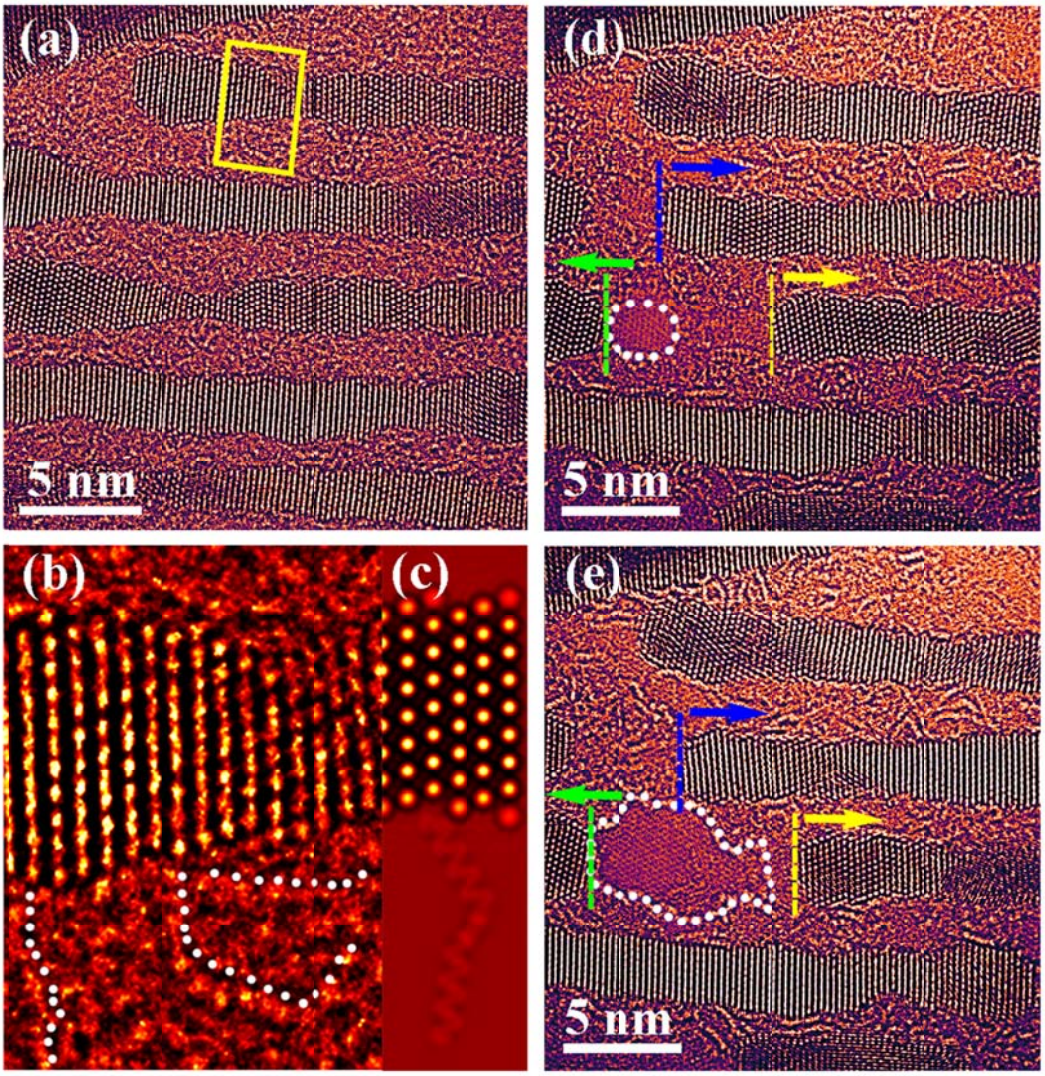

Figure 3. Surface ligands of ultrathin Au NWs. (a) AC-HRTEM image of several well-aligned NWs and surface ligands in between. (b) Enlarged image of the boxed region in (a). Chain-like features are indicated by the dot lines. (c) Simulated image of single oleylamine ligand on ultrathin Au NW surface. (d,e) In-situ observation of the evolution of surface chain-like features accompanied by the NWs breaking and moving. Arrows indicate the moving directions of the NW tips. The dot line surround regions are single layer graphene membrane.

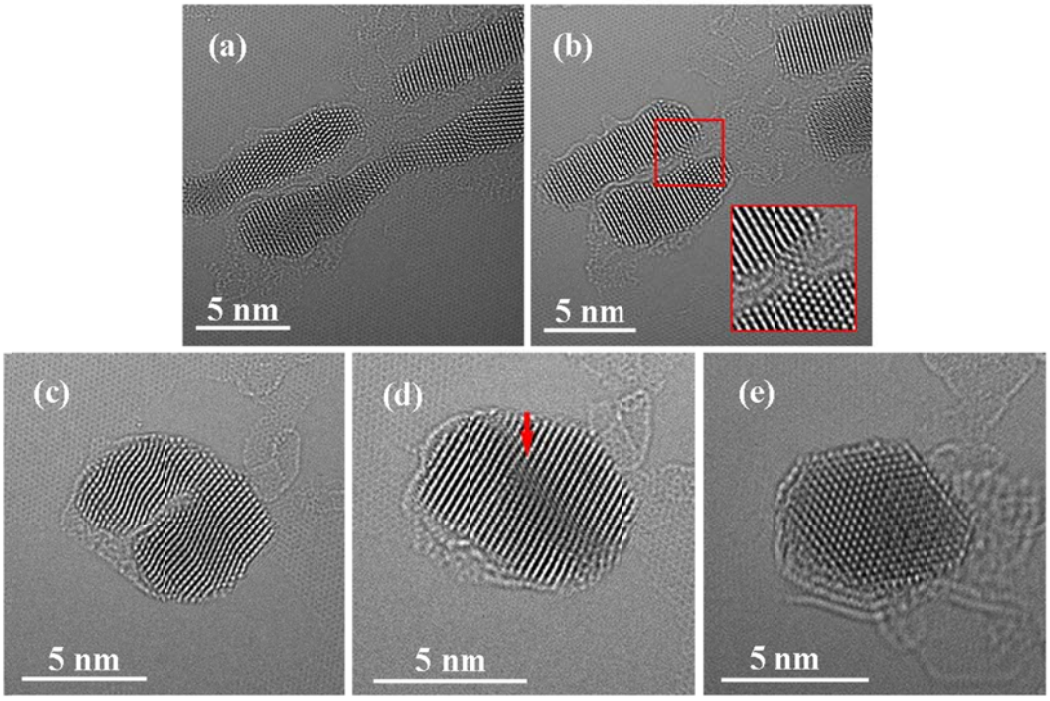

Figure 4. Coalescence of ultrathin Au NWs via in-situ AC-HRTEM observation. Inset in (b) is the enlarged image of the boxed region, clearly showing the atomic channels of surface diffusion. The arrow in (d) indicates a dislocation.

TOC